

Optical excitation of bulk plasmons in n-doped InAsSb thin films : investigating the second viscosity in electron gas

Antoine Moreau,^{1,*} Émilie Sakat,² Jean-Paul Hugonin,³ Téo Mottin,¹ Aidan Costard,¹ Denis Langevin,¹ Patricia Loren,⁴ Laurent Cerutti,⁵ Fernando Gonzalez Posada Flores,⁵ and Thierry Taliercio^{5,†}

¹Université Clermont Auvergne, CNRS, Institut Pascal, F-63000 Clermont-Ferrand, France

²Université Paris Saclay, Center for Nanoscience and Nanotechnology, C2N UMR9001, CNRS, 91120 Palaiseau, France

³Université Paris-Saclay, Institut d'Optique Graduate School, CNRS, Laboratoire Charles Fabry, 91127 Palaiseau, France

⁴Institut de Physique de Nice, CNRS, Université Côte d'Azur, 06200 Nice, France

⁵Institut d'Electronique et des Systèmes, CNRS, Université de Montpellier, 34095 Montpellier, France

(Dated: December 3, 2024)

We demonstrate that including the second viscosity of an electron gas in the hydrodynamic model allows for highly accurate modeling of the optical response of heavily doped semiconductors. In our setup, which improves resonance visibility compared to previous approaches, plasmon resonances become more distinct, allowing for detailed analysis of the underlying physics. With advanced fitting techniques based on a physics-informed cost function and a tailored optimization algorithm, we obtain close agreement between simulations and experimental data across different sample thicknesses. This enhanced resonance visibility, combined with our integrated approach, shows that key parameters such as doping level and effective electron mass can be retrieved from a single optical measurement. The spatial dispersion taken into account in the hydrodynamic framework is essential for accurately describing the optical response of plasmonic materials in this frequency range and is likely to become a standard modeling approach.

The optical response of highly n-doped semi-conductors is essentially dictated by the response of the free electron gas, which is usually and effectively described using a simple Drude model[1]. This model assumes no interactions between electrons within the gas. However, since the early work of Tonks and Langmuir in the 20th century[2], it has been established that electron gases can also support plasmons – longitudinal electromagnetic waves similar to sound. Accurately modeling these waves requires moving beyond the Drude model to include electron-electron repulsion at the scale of the mean free path typically, which introduces spatial dispersion, or nonlocality, into the description.

Near the plasma frequency, even a single slab of doped semiconductors exhibits resonances. These resonances, first predicted for thin metal films by Ferrell[3] using the Drude model, can be optically excited and are now routinely employed to characterize doping levels in semiconductors[4].

Melnyk and Harrison[5] have been the very first to suggest that longitudinal waves are actually excited inside the slab and are responsible even for the Ferrel resonance. They provided a theoretical framework to describe the response of a metallic slab that is still relevant nowadays[6]. Using Maxwell's equations and a simple hydrodynamic model for the electron gas, they predict that plasmon resonances should occur in a metallic film just above the screened plasma frequency, for which the permittivity vanishes. They even suggest that this could happen for doped semi-conductors as well. Such resonances can be considered as cavity resonances for plasmons, with some peculiar characteristics however.

Only recently has the scientific community started to realize the importance of nonlocality in doped

semiconductors[7]. Recent experiments have shown resonances linked to the excitation of plasmons in semiconductor films of 20 nm or less in thickness[8], amid a debate on the origin of the supplementary losses experienced by plasmons[9], beyond those due to friction with the lattice. Such resonances, observed in quantum wells, have also been and described using a fully quantum approach to the electron gas[10]. We underline that spatial dispersion can have an impact also below the (screened) plasma frequency for guided modes with a large wavevector, as is common in plasmonics. Therefore, investigating the effects of nonlocality is crucial for a deeper understanding and a more accurate modeling of these phenomena.

In this work, we demonstrate that cavity resonances for plasmons can be observed in doped semiconductors that are nearly an order of magnitude thicker than those previously studied[8]. In order to do so, we illuminate our sample using a high index germanium prism, in a relatively symmetrical configuration which enhances the visibility of the resonances. We provide new physical insights to better understand their characteristics. By utilizing advanced numerical fitting techniques, we show that the experimental spectra can be almost perfectly replicated using the formalism inspired by the hydrodynamic model[11]. Importantly, we show that taking into account the bulk viscosity of the electron gas results in an imaginary part of the nonlocal parameter β^2 [8, 9, 12], and that this is necessary to reach a satisfactory agreement with experimental data.

Our results suggest that accounting for spatial dispersion can enable the accurate determination of the electron gas characteristics, such as its density, the effective mass of electrons and more, in a single optical measurement.

In the first part of this paper, we review the basics of spatial dispersion in an electron gas and the characteristics of plasmons to provide a foundation for a more thorough dis-

* antoine.moreau@uca.fr

† thierry.taliercio@umontpellier.fr

discussion of our results. We then detail our experimental findings, demonstrating how the observed resonance positions align with predictions from the hydrodynamic model. In the third section, we explain how the use of a global optimization algorithm and an adapted cost function to fit our experimental data allows to retrieve all the model parameters. The final section is dedicated to an in-depth discussion of the overall implications of our results.

I. THEORETICAL FRAMEWORK

A. Hydrodynamic model

Drude's model is first based on the idea that the volume current density \mathbf{j} can be integrated as a screened polarization \mathbf{P}_f of the medium, using the relation $\mathbf{j} = \frac{\partial \mathbf{P}_f}{\partial t}$. A metal or a doped semi-conductor with a free carrier gas can thus always be described with such an effective polarization. In the framework of the Drude model, the link between this polarization and the electric field can be written

$$\frac{\partial^2 \mathbf{P}_f}{\partial t^2} + \gamma \frac{\partial \mathbf{P}_f}{\partial t} = \varepsilon_0 \omega_p^2 \mathbf{E}, \quad (1)$$

where γ accounts for the friction of the electron gas against the lattice and $\omega_p^2 = \frac{n e^2}{m^* \varepsilon_0}$, n being the density of the electron gas and m^* the effective mass of electrons.

It should be underlined that the effective polarization, in the harmonic regime (we assume a $e^{-i\omega t}$ time dependency here), is actually proportional to the displacement of the electrons (or carriers more generally) with respect to their average position. The second term is linked to the friction of the electrons on the lattice, while the last is the electric force. In the harmonic regime, the displacement of the electrons is always opposite to the electric force because there is no other restoring force. The effective polarization is thus opposite to the electric field and dominates if the frequency is low enough, making the permittivity negative.

The rest of the medium is characterized by a susceptibility χ_b that may depend on the frequency. In the framework of the Drude model, the permittivity of the material is thus given by

$$\varepsilon = \varepsilon_0 \left(1 + \chi_b - \frac{\omega_p^2}{\omega^2 + i\gamma\omega} \right). \quad (2)$$

The screened plasma frequency, for which the real part of the permittivity vanishes, is given approximately by

$$\omega_0 = \frac{\omega_p}{\sqrt{1 + \chi_b}}. \quad (3)$$

It is called the screened plasma frequency or the epsilon-near-zero (ENZ) frequency in the following because below this frequency the semiconductor can be considered as a plasmonic material, like metals in the visible range. Although many authors use "plasma frequency" to describe the ENZ

frequency, these two frequencies must be distinguished, particularly given the high susceptibility of semiconductors in the infrared range (typically, $\chi_b \simeq 10$).

It should also be noted that the actual plasma frequency ω_p cannot be measured directly. Experimental measurements always yield the screened plasma frequency ω_0 , as the response of the surrounding medium is inherently included in any optical observation.

The hydrodynamic model [13] is the simplest possible way to take into account the repulsion between electrons, by integrating a pressure term in the description of the electron gas response. This leads to the following relation between the electric field and the effective polarization:

$$\frac{\partial^2 \mathbf{P}_f}{\partial t^2} + \gamma \frac{\partial \mathbf{P}_f}{\partial t} - \beta^2 \nabla(\nabla \cdot \mathbf{P}_f) = \varepsilon_0 \omega_p^2 \mathbf{E}. \quad (4)$$

The electron pressure term $\beta^2 \nabla(\nabla \cdot \mathbf{P}_f)$, coming from the Thomas-Fermi theory of metals, obviously includes spatial derivatives of the polarization, making the description non-local. We underline that the continuity equation can be written $\nabla \cdot \mathbf{P}_f = -\rho$ in this framework, so that this supplementary term truly appears as a force pushing electrons away from any concentration of negative charges.

The parameter β quantifies the non-local effects and is called the hydrodynamic parameter. It is usually defined as $\beta = \sqrt{3/5} v_F$ with $v_F = \frac{\hbar}{m^*} (3\pi^2)^{1/3} n_0^{1/3}$, the Fermi velocity [13]. The coefficient between β and v_F actually depends on the frequency. However, close to the screened plasma frequency $\sqrt{3/5}$ is a very accurate assumption [12].

Whatever the medium considered, the electric field can always be decomposed as the sum of a divergence-free component (the transverse wave) and a curl-free component (the longitudinal wave) [14]. Since the divergence of the magnetic field is always null, the magnetic field always belongs to the purely transverse part of the decomposition. The two kinds of waves evolve independently from each other – in the sense that the transverse wave is never converted into a longitudinal one along its propagation in a homogeneous medium. The transverse wave is completely insensitive to spatial dispersion, it is described as a wave propagating in a local medium with a permittivity given by the Drude model. We underline generally that while classical electromagnetic theorems can be extended to spatially dispersive media, their generalization is not straightforward [15].

At an interface between the non-local medium and any local medium, the component of the current perpendicular to the interface vanishes, which is simply given in the harmonic regime by $\mathbf{P}_f \cdot \mathbf{n} = 0$ and provides the necessary additional boundary condition [16, 17].

When light from a local medium illuminates an interface, the two types of waves (transverse and longitudinal) can be excited within the nonlocal medium. The boundary conditions determine the amplitude of these waves. More specifically, the strength of the longitudinal wave excitation depends on the direction of the electric field at the interface. At normal incidence, with the electric field purely tangential to the surface, the longitudinal wave remains unexcited, but as

the incidence angle increases, the excitation of the longitudinal wave becomes stronger.

When a longitudinal wave inside a nonlocal material encounters an interface with a local material, it is reflected, but a transverse wave is also excited in the process. This phenomenon is best described using a scattering matrix formalism[11] adapted to the hydrodynamic model, which we employ here to calculate the reflectance of any given structure.

In what follows, we will use the term plasmon to refer to the longitudinal wave, though technically, a plasmon is the quantum of this wave. The transverse wave will simply be referred to as light.

The dispersion relation of the plasmon, taking into account losses due to friction with the lattice, can be written as[16]:

$$\omega^2 + i\gamma\omega = \omega_0^2 + \beta^2\mathbf{k}^2, \quad (5)$$

while the dispersion of light inside the nonlocal medium can be written as:

$$\omega^2 = \omega_0^2 + \frac{c^2}{1 + \chi_b}\mathbf{k}^2. \quad (6)$$

As the Fermi velocity and thus β is much smaller than the speed of light, this means that, above ω_0 , the wavevector of plasmons is a few orders of magnitude larger than that of light (whether in vacuum or inside the medium).

An example of dispersion curve for the plasmon is shown in Figure 1. The parameters chosen here are in agreement with the experiments and data fits presented in the third section. Below the screened plasma frequency ω_0 , plasmons are evanescent, just as light. Their wavevector being essentially imaginary, it is possible to define a typical penetration depth δ_p for these waves. It is usually much shorter for plasmons than for light. All accounted for, this typical length is proportional to $n_0^{-1/6}m^{*-1/2}$, thus decreasing with the electronic density. In highly-doped semiconductors the free carrier density n_0 is orders of magnitude lower than in noble metals and the effective mass m^* is also lower – this explains why $\omega_p = \sqrt{\frac{n_0 e^2}{m^* \epsilon_0}}$ is in the infra-red range.

However, these considerations show that theoretically, the plasmon skin depth δ is at least 5 times larger or more in highly-doped semiconductors than in noble metals. This constitutes another indication that non-local effects can be expected to play a much larger role in the semiconductors response, even below the screened plasma frequency, because of its lower carrier density.

Different authors have considered that the parameter β should be taken complex and frequency-dependent, on very different physical grounds. For Halevi, the reasons lie in the microscopic model[12] that underpins the hydrodynamic model. In the Generalized Nonlocal Optical Response (GNOR) model, a supplementary diffusion term is considered[9], while it has been shown more recently that accounting for viscosity within the electron gas also results in a complex β with a different frequency dependence[8]. To summarize, while there is consensus on the necessity of an imaginary component for β , its origin and physical meaning remain debated to this date.

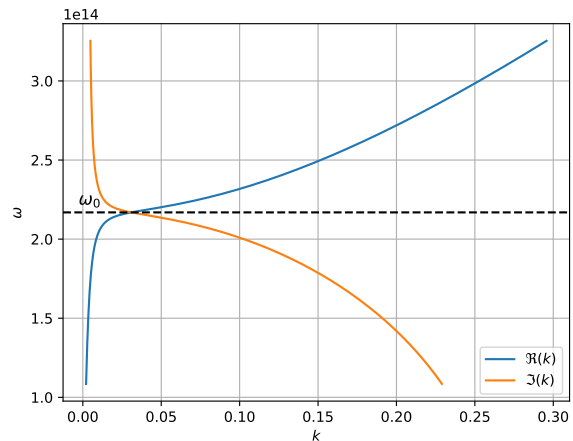


FIG. 1. Dispersion curve for the plasmon with $\omega_0=2.169 \cdot 10^{14}$ $\text{rad}\cdot\text{s}^{-1}$, $\gamma=5.901 \cdot 10^{12}$ $\text{rad}\cdot\text{s}^{-1}$, $\beta = 8.2019 \times 10^5$ $\text{m}\cdot\text{s}^{-1}$. For $\omega > \omega_0$ the plasmon becomes propagative, showing a wavevector that is essentially real, while it is evanescent for $\omega < \omega_0$ with a dominant imaginary part.

B. Resonances in a metallic slab

In the Drude model, the very first step is to treat the currents inside the free electron gas as an effective polarization. This can be done easily because oscillating dipoles also correspond to real microscopic currents. The second step is to assume that free electrons oscillate independently under the influence of the incoming electric field.

Within this framework, when a horizontal slab containing a free electron gas is illuminated in normal incidence, the gas is free to oscillate horizontally. No resonance is associated to such an oscillation. Depending on whether the frequency is larger or smaller than the screened plasma frequency, the horizontal oscillation will allow the electric field to penetrate inside the slab or not, respectively.

When the angle of incidence is different from zero, a vertical oscillation is predicted to occur at exactly the screened frequency ω_0 when the electric field penetrates the entire slab. For a rigid gas to oscillate vertically, charges must accumulate on both surfaces of the slab, creating a restoring force that drives the oscillation and induces a resonance. This mechanism has been suggested by Ferrell initially[3]. Shortly thereafter, a resonance has been observed more or less in the predicted conditions[18] and it is sometimes said that it corresponds to the excitation of a so called Brewster mode. There is however no guided or cavity mode that is excited in that case. The nature of the resonance is fundamentally different from a cavity resonance for light, or of the excitation of a guided mode.

When interactions between electrons are considered, a different picture emerges[5, 6], which can be considered more accurate and more complete. Surface charges can no longer be described as such; instead, they appear as volume charges near the surface, a phenomenon known as 'smearing' of the

charges. The electron gas can no longer be viewed as a rigid entity moving as a whole; rather, it supports plasmons.

When a plasmon is excited by incident light, the wavevector component along the interface is conserved. However, the plasmon's wavevector is much larger than that of light, as discussed earlier. As a result, the plasmon's wavevector is dominated by its vertical component, regardless of the incidence angle. The slab can therefore be treated as a cavity for these waves, with resonances occurring at relatively small thicknesses. Melnyk and Harrison's calculations[5] demonstrate that only odd-order resonances can be excited. Although the fundamental resonance is more pronounced and was initially thought to confirm Ferrell's mechanism, experiments – first with potassium in the 1970s[19], and more recently with thin films of highly doped semiconductors[8] – have observed higher-order resonances that are not consistent with Ferrell's interpretation. This confirms that the metallic slab behaves as a plasmon cavity, supporting odd resonances, and that a spatially dispersive model is required for an accurate description of its response.

II. EXPERIMENTAL RESULTS

A. Sample preparation

We have prepared two series of samples of Si doped n-InAsSb, which we will denote #1 and #2. The two series differ by their doping level. Each series derives from a single 204 nm thick n-InAsSb which is subsequently etched to guarantee both an homogeneous level of doping in each series and a good control of the thickness.

The initial samples were grown using a RIBER-C21 solid source molecular beam epitaxy tool on n-doped ($1 - 2 \times 10^{18} \text{ cm}^{-3}$) GaSb substrates. Prior to the growth process of the n-InAsSb layer, a thermal desorption step is performed to remove the native oxide and a 210 nm thick buffer layer of undoped GaSb is grown to smooth the surface and bury any impurities remaining after deoxidation.

The n-InAsSb layer is a digital alloy, i.e. a short period superlattice, which allows the deposited thickness, 204 nm, to be accurately monitored for both samples. The doping level of the Si doped n-InAsSb layer, estimated using the optical method described in [4], is of $5.3 \times 10^{18} \text{ cm}^{-3}$ and $1.20 \times 10^{19} \text{ cm}^{-3}$ for sample #1 and #2, respectively. The determination of the doping level, as mentioned above, is a reflection experiment under polarized light with an angle of incidence of 60° . A home-made abacus then allows to deduce the carrier density from the measurement of the resonance wavelength.

The initial samples are broken into several pieces and each one is then etched to obtain a series of samples, with a thickness varying from 7 nm to 204 nm. The samples are wet etched at 20°C in a 2:1 ratio of citric acid ($\text{C}_6\text{H}_8\text{O}_7$) and hydrogen peroxide (H_2O_2) solution, the time of exposition allowing to control the final thickness. To evaluate the final thickness of each sample, a part of the surface is protected from wet etching by a small drop of photoresist (AZMIR-701) deposited on one edge and heated at 90°C for 1 min 30 s. After

removal of the photoresist, the remaining step is measured by atomic force microscopy (AFM) and subtracted from the total thickness of 204 nm. The resulting thicknesses, despite similar exposure time, differ for series #1 and #2.

B. Optical response measurement

A typical reflectance spectrum is shown in Figure 2 (black line) for sample #2. The dip in the reflectance that can be observed around $9 \mu\text{m}$ corresponds to the excitation of the main plasmon resonance inside the InAsSb layer.

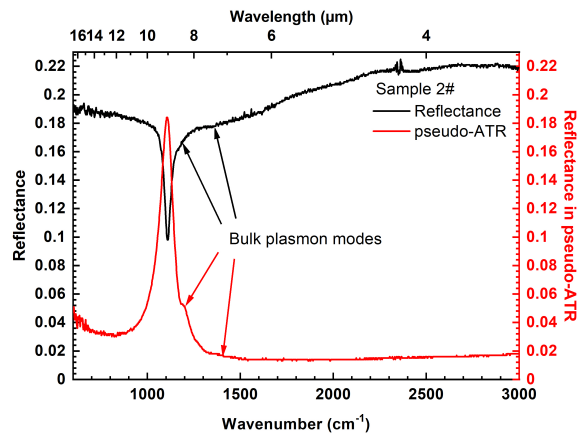


FIG. 2. Reflectance spectrum under p-polarized light with an angle of incidence of 60° (black line) and pseudo-ATR spectrum of sample #1 with a thickness of 204 nm.

This resonance can be excited either in reflection, when illuminated from air, or when illuminated from inside a germanium crystal using a Schwarzschild objective, mounted on a microscope (Hyperion 3000) and coupled to an FTIR spectrometer (Bruker, Vertex 70). Given the high index of the Ge crystal (around 4), such a configuration amounts to exciting the structure using a prism, with an angle of incidence between 21.5° and 37° , determined by the objective (see Fig.3). For media with a refractive index smaller than 1.6, this means total internal reflection will occur and this would constitute an attenuated total internal reflection (ATR) setup. However, especially in the mid-IR range, materials most often present larger indexes so that we call this configuration "pseudo-ATR" in the rest of the paper.

The pseudo-ATR spectrum of sample #2 is the red curve in Figure 2, showing that the fundamental plasmon resonance leads to a reflectance peak. Furthermore, this allows to observe supplementary resonances that are more easily spotted in pseudo-ATR configuration but that can also be found in the reflectance when illuminating the structure from air, when the spectrum is very closely analyzed. This underlines one of the main contributions of our work: when the doped semi-conductor is sandwiched between two materials (Ge and GaSb) with large and close refractive index, plasmon resonances are much easier to observe than in any other con-

figuration.

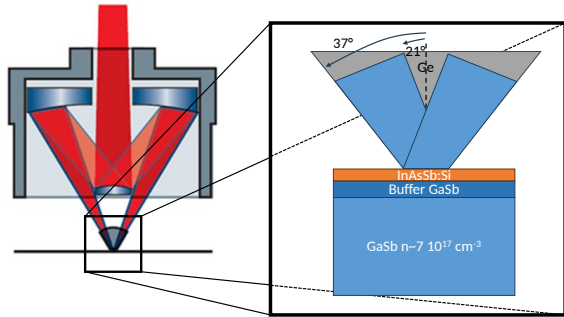


FIG. 3. Experimental setup in the pseudo-ATR configuration. The sample is illuminated with incidence angle ranging from 21° to 37° .

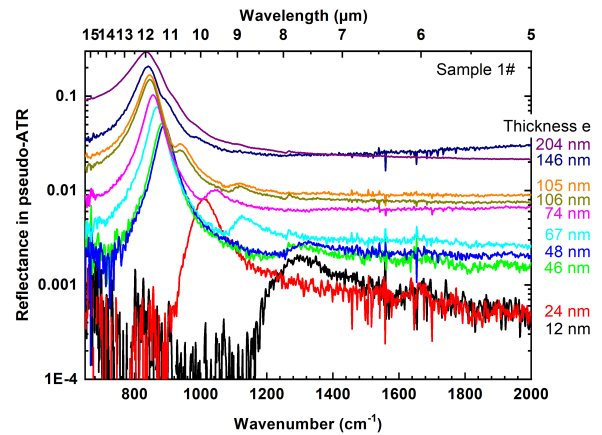


FIG. 4. Pseudo-ATR spectra for several thickness of sample #1.

C. Plasmon resonances

Using the samples of different thicknesses, we first map the resonances that can be seen on the different spectra shown in Figure 4 and Figure 5 and compare the position with predictions provided using a hydrodynamic model.

The pseudo-ATR spectra of series #1 are shown in Figure 4 in log scale. Spectra are background corrected with a reference sample of GaSb with a 210 nm thick buffer layer of undoped GaSb. In each spectrum the fundamental plasmon resonance (that we often call Ferrell resonance) can be seen at short wavelength and it progressively blueshifts when the thickness decreases. We identify this peak as the first order plasmon mode, $\ell = 1$. At higher wavelengths, some additional peaks corresponding to the odd high order plasmon modes, $\ell = 3, 5, 7, \dots$ can be observed, even if higher order resonances can be difficult to identify. All these resonances also blueshift with decreasing thickness. Such a behaviour can be expected for plasmon resonances as will be explained below. Such a blueshift is however not found for the Ferrell resonance in the framework of the Drude model. Note that the small peak at 1250 cm^{-1} is due to the GaSb substrate. To accurately extract the wavenumber of each high order bulk plasmon mode, we first fit the first order bulk plasmon with a Lorentzian function, which we subtract to the experimental data.

The position of the resonances as a function of the sample thickness is summarized in Figure 5. The colored disks correspond to the wavelength of the bulk plasmon modes, white, red, blue and pink for $\ell = 1, 3, 5$ and 7 respectively. Error bars on the disk position are indicated with vertical and horizontal lines.

All bulk plasmon modes blueshift with decreasing thickness. This result is confirmed by the simulation of the spectra using the HDM described above. The color map in Figure 5 corresponds to $\log_{10}((\text{RHDM}(s) + \text{RHDM}(p))/2)$ where $\text{RHDM}(s)$ and $\text{RHDM}(p)$ are respectively the pseudo-ATR spectra under s- and p-polarizations. Experiments and simulations agree relatively well. We have used the same parameters for both samples to model the n-type GaSb substrate

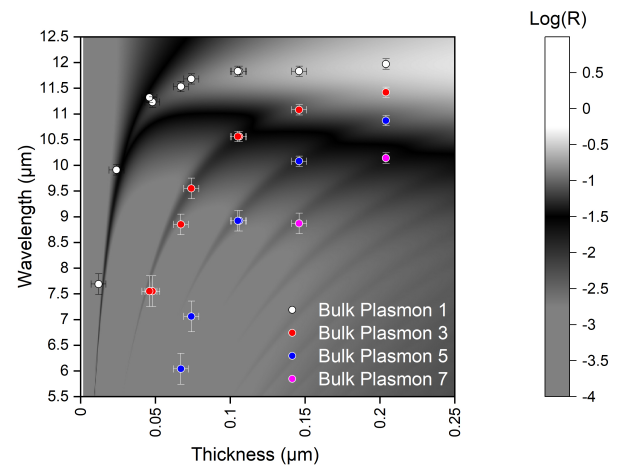


FIG. 5. Plot of the simulated spectra of $\log_{10}((\text{RHDM}(s) + \text{RHDM}(p))/2)$ where $\text{RHDM}(s)$ and $\text{RHDM}(p)$ are the pseudo-ATR spectra under s- and p-polarizations respectively. The colored disks correspond to position of the plasmon resonances as determined using the experimental data. We identify each resonance with an odd number. Error bars are the vertical and horizontal ticks for each disk.

and the GaSb buffer. The n-type GaSb substrate is correctly modelled with a Drude model using parameters $\epsilon_\infty = 14.4$, $\omega_p = 2.2 \times 10^{14} \text{ rad.s}^{-1}$, and $\gamma = 5 \times 10^{12} \text{ rad.s}^{-1}$. For the GaSb buffer we used the refractive index in [20]. For the n-InAsSb layer, the fitting parameters of the HDM are the carrier density, $n_0 = 5.5 \times 10^{18} \text{ cm}^{-3}$, the damping parameter, $\gamma = 6.4 \times 10^{12} \text{ rad.s}^{-1}$ and the hydrodynamic parameter, $\beta = 8.95 \times 10^5 \text{ m.s}^{-1}$.

The same study is carried out on sample #2. Figure 6 is the pseudo-ATR spectra for different thicknesses. As the sample presents a higher level of doping, the first order of the bulk plasmon mode is blueshifted compared to sample #1. The resonances are also broadened. However, it is possible to observe the high order bulk plasmon modes up to $\ell = 11$. Once

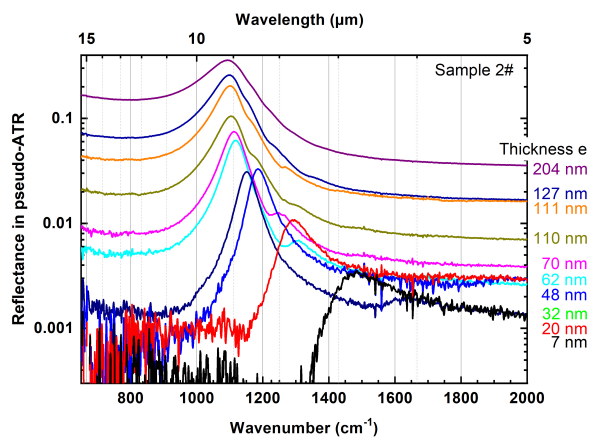


FIG. 6. Pseudo-ATR spectra for several thicknesses, for sample series #2.

all the odd orders of the bulk plasmon mode were extracted, we carried out a fit with the HDM to get the parameters of the sample #2 (Fig. 7).

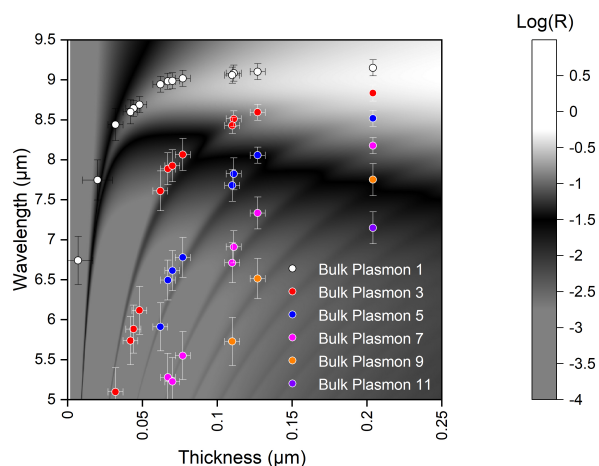


FIG. 7. Plot of the simulated spectra of $\log_{10}((\text{RHDM}(s) + \text{RHDM}(p))/2)$. The colored disks correspond to the order of the bulk plasmon modes. Error bars are the vertical and horizontal ticks for each disk.

The behaviour of the bulk plasmon modes is the same as for sample #1. Once again, the experiments and simulations agree quite well. We have used the following fitting parameters of the HDM to describe the n-InAsSb layer: the carrier density, $n_0 = 1.2 \times 10^{19} \text{ cm}^{-3}$, the damping parameter, $\gamma = 8 \times 10^{12} \text{ rad.s}^{-1}$ and the hydrodynamic parameter, $\beta = 9.29 \times 10^5 \text{ m.s}^{-1}$.

III. IMPROVED PARAMETER RETRIEVAL

As demonstrated by the results above, the pseudo-ATR configuration significantly enhances the response of semi-

conductor slabs, allowing us to accurately determine the parameters of the hydrodynamic model, which is usually challenging[21]. To streamline this process, we have developed an automated method to retrieve these parameters. Our method includes three key components. Firstly, we use the hydrodynamic model with a complex hydrodynamic parameter β , which will be explained in detail below. Secondly, we define a cost function that prioritizes matching the overall shape of the curves rather than just minimizing the distance between data points, aligning better with the intuitive assessment of physicists. Thirdly, we employ the Differential Evolution (DE) global algorithm, known for its efficiency in solving physical problems[22, 23], ensuring that we do not miss any satisfactory parameter values.

The experimental results in the pseudo-ATR configuration cover a wide range of incidence angles, from 21.5° to 37° , with no means to determine the respective weight of each angle. However, as shown in Figure 8, the response of the semiconductor slab strengthens and the visibility of the plasmon resonances improves with increasing incidence angle. We also note that the overall shape of the signal remains fairly consistent. Therefore, we assume that the spectrum corresponding to the largest angle likely dominates the experimental results. We thus fit the data to the simulation results using only the largest incidence angle, but we do not expect a good match below ω_0 since the reflectance for the lower incidence angle is nearly the same as for the highest. We thus expect the single-angle simulation to underestimate the reflectance for large wavelengths.

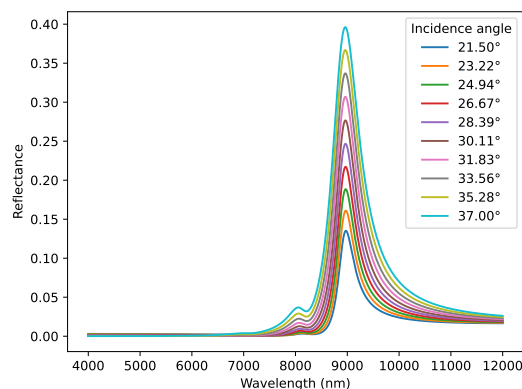


FIG. 8. Simulations showing the dependence of the reflectance spectrum with respect to the incidence angle for angles ranging from 21.5° to 37° for a 70 nm thick InAsSb.

We first chose to fit the experimental data using parameters that rely minimally on underlying assumptions and can be considered empirical, such as χ_b , ω_p , and γ for the Drude model, and a complex value of β for the hydrodynamic part. To accurately fit the experimental data, we also include a parameter for the background signal and another for scaling the data.

In addition, we have fitted our data with a dispersive imaginary part for the complex value of β^2 , which will be justified

thoroughly below. The complex value of β^2 is denoted by η^2 and can be expressed as:

$$\eta^2 = \beta^2 - i\omega \frac{\xi}{n_0 m^*}. \quad (7)$$

Here ξ is an additional parameter whose origin will be explained later.

The cost function is given by

$$f(\Pi) = \frac{1}{N} \sum_{i=1}^N |R(\lambda_i) - S(\Pi, \lambda_i)| + N \times \frac{1}{N-1} \sum_{i=1}^{N-1} |(R(\lambda_{i+1}) - R(\lambda_i)) - (S(\Pi, \lambda_{i+1}) - S(\Pi, \lambda_i))| \quad (8)$$

where λ_i is a wavelength for which a reflectance $R(\lambda_i)$ has been measured, Π represents the parameters of the simulation ($\chi_b, \omega_p, \gamma, \beta, \frac{\xi}{n_0 m^*}$, background signal intensity, scaling parameter), and $S(\Pi, \lambda_i)$ is the reflectance of the structure simulated for the given parameters and wavelength.

The second term in the cost function guides the optimization to minimize differences in the derivatives of the experimental and simulated reflectance curves. While the experimental signal $R(\lambda)$ naturally includes noise that increases the cost function's value, this noise does not alter the position of the minimum in the parameter space, ensuring the robustness of the optimization process.

In order to find the minimum of the cost function, we use Differential Evolution (DE) (more precisely its Quasi-Optimizational version[23]) to look for satisfactory values of the parameters. DE is a non-deterministic algorithm and can be expected to provide different results each time it is run. We also take the results of DE and then perform a steepest descent[23], in order to be sure we have reached a local minimum.

The numerical computation of the reflectance, taking into account an imaginary part for β^2 , has been included in the open source PyMoosh software[24]. In addition, we have made examples available with the code under the form of a Jupyter notebook, leveraging the features of PyMoosh to retrieve the parameters of the model efficiently[25].

The resulting fits are particularly satisfactory despite the uncertainty in the incidence angle and the lack of any averaging. An example is shown Fig. 9 a 70 nm thick sample from series #2, where the plasmon resonances are clearly visible. These fits have been obtained by assuming a constant imaginary part for η^2 . This shows how accurately the hydrodynamic model with a complex value for η^2 is able to model the response of the semiconductor.

The importance of the imaginary part of the β parameter is illustrated in Figure 10. As the imaginary part increases from zero to $8 \times 10^{13} \text{ m}^2 \cdot \text{s}^{-2}$, the resonance profile changes drastically. When β is real, the resonance exhibits a clear Fano profile, indicating strong coupling of the slab to the continuum on both sides – which can be linked to our experimental setup. However, as the imaginary part grows, the profile becomes smoother. This significant change in the profile allows for a rather accurate estimation of the imaginary part,

plained later.

The cost function we chose is a linear combination of (i) the difference between the model and the experimental data, as is usual, and (ii) the difference between the slopes of the model and the experimental data, normalized. Including the difference in slopes as a criterion results in a model curve that may be shifted but maintains the same overall shape, aligning with what a physicist would intuitively aim for.

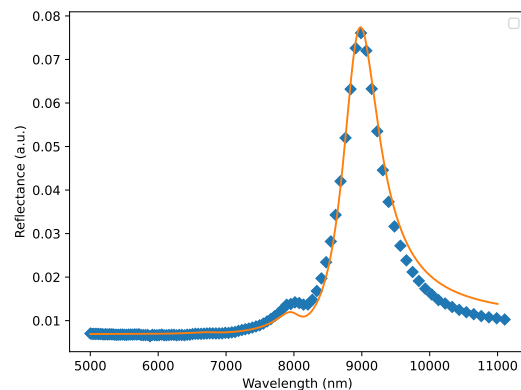


FIG. 9. Reflectance as a function of wavelength for a semiconductor slab from series #2 with a thickness of 70 nm. The observed plasmon resonances align closely with the model, demonstrating the accuracy of the hydrodynamic fit using a complex η^2 with an imaginary part (the imaginary part is constant here).

for which a value of zero can be completely excluded.

The parameter retrieval can be performed on a single spectrum for a given thickness or across multiple thicknesses. Based on our experience, a fit on a single spectrum is sufficient when the main resonance and at least one higher-order resonance are clearly visible. The more resonances that are observable, the better the determination of β . For sample #2, selecting a spectrum with enough resonances yielded the most reliable results. For instance, using the spectrum for a 100 nm thickness (shown in Fig. 11), we obtained estimations of $n_0 = 1.39 \times 10^{19} \text{ cm}^{-3}$, $m^* = 0.077 m_0$ and $\xi = 5.7 \times 10^{-10} \text{ Pa.s}$.

However, to get more reliable values, a fit taking into account all the thicknesses can be preferable. At small thicknesses, the shift of the main resonance away from ω_0 is directly linked to the value of β , thus providing important in-

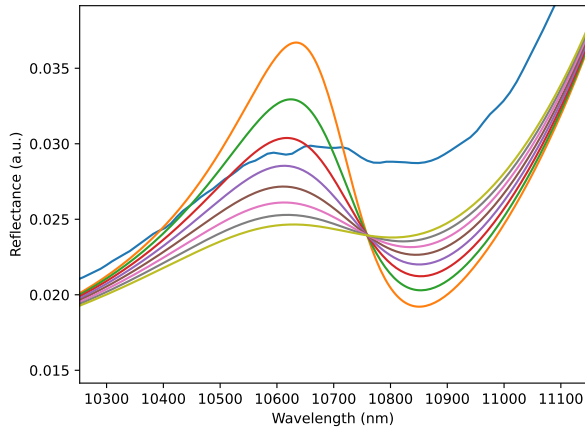


FIG. 10. Resonance characterized by $\ell = 3$ for a 106 nm thick sample of series #1, for different values of $\frac{\xi}{n_0 m^*}$ ranging from 0 to 7×10^{-4} in $\text{m}^2 \cdot \text{s}^{-1}$. The orange curve corresponds to $\xi = 0$. When the value of ξ increases, the resonance profile becomes smoother and deviates from a Fano profile.

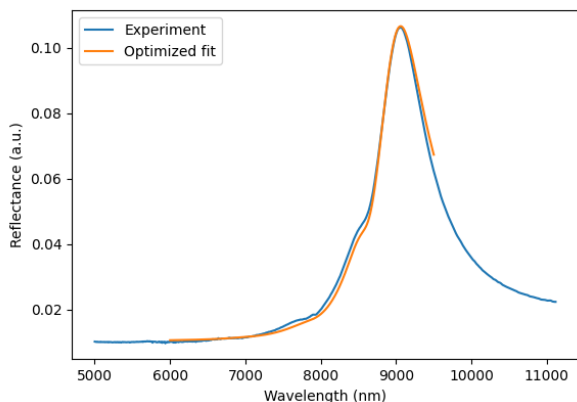


FIG. 11. Experimental reflectance data for a 110 nm thick InAsSb layer of sample #2 in the pseudo-ATR configuration, compared with the best fit obtained for the given model parameters. The optimized fit is displayed only within the wavelength range used for optimization.

formation for the optimization. For sample #1, the results are very convincing, as shown Fig. 12. The values obtained are $n_0 = 5.31 \times 10^{18} \text{ cm}^3$, $m^* = 0.057 m_0$ and $\xi = 2.11 \times 10^{-10} \text{ Pa.s}$.

We underline that the optimization terminates with a steepest descent but still provides slightly different results each time. This means the cost function has many local minima and that the problem, from the optimization point of view, is challenging. This produces uncertainty in the values provided for the parameters of the model, and consequently for the estimation of n_0 , m^* and ξ .

Especially, even small variations in the estimation of β result in a relatively large (around 10%) variation in the estima-

tion of n_0 . Conversely, the value provided for the effective mass of the electron is much more stable. Comparing these results with a manual retrieval as shown Sec. II C is a good idea, but we are confident given the present results that with a more controlled incidence angle or a more precise determination of the thickness of each sample, the accuracy of the whole process can be improved.

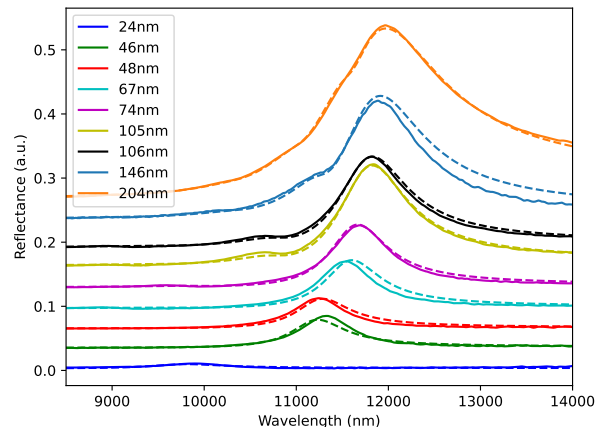


FIG. 12. Experimental reflectance data (solid lines) for several thicknesses and the result of a global fit (dashed lines) on all the curves at once for sample #1. The curves are shifted vertically to be more clearly visible. The values provided by the optimization are $n_0 = 5.31 \times 10^{18} \text{ cm}^3$, $m^* = 0.057 m_0$ and $\xi = 2.11 \times 10^{-10} \text{ Pa.s}$.

IV. DISCUSSION

A. The slab as a two mode cavity

The model proposed by Ferrel, which describes the electron gas as somewhat rigid, is appealing due to its simplicity. The picture of a cavity for longitudinal waves is however much more accurate and powerful, and we will detail all its aspects here.

In that framework, it is easy to estimate the position of the resonances. Given the large value of the wavevector for plasmons, even when its component along the interface k_x increases, the normal k_z component remains essentially unchanged. Whatever the incidence angle, the plasmon can thus be considered to propagate almost perfectly perpendicularly to the interfaces. The resonance condition for such a cavity can be expressed as:

$$k = \frac{\ell\pi}{h} \quad (9)$$

where ℓ is a non zero integer, h the thickness of the slab and k the plasmon wavevector. Using the lossless dispersion relation for the plasmon, this provides an approximation for

the resonance frequencies:

$$w_m = \sqrt{w_0^2 + \left(\frac{\ell\beta\pi}{h}\right)^2}. \quad (10)$$

Despite its simplicity and the fact that the losses are neglected, this formula is quite accurate, as shown in Fig. 13, where the lossless dispersion relation is used to compute the position of the resonance on the spectrum. The spectrum shown is computed with $\xi = 0$ to better see the position of the resonances. The figure shows clearly that only the resonance corresponding to an odd value of ℓ can be seen. We discuss below how the cavity picture is able to explain also this characteristics.

The accuracy of formula (10) justifies the assumptions that the incidence angle or the losses have little impact on the position of the resonances – except for the fundamental one because the dispersion relation for the plasmon including losses significantly differs for low wavevectors, as shown in Fig. 1.

Of course, the amplitude of each resonance is dependent on the incidence angle. In the Ferrel picture and in the Drude model framework, it cannot be excited in normal incidence because it is a vertical oscillation. In the cavity picture, it is not excited in normal incidence because the electric field associated to the plasmon needs a component perpendicular to the interface to be excited.

The cavity picture allows to understand why the first resonance does not occur exactly at ω_0 , if ω_0 is defined as the frequency for which the real part of the permittivity vanishes. As shown in Figure 13, there is a shift between the position of the first resonance predicted by the hydrodynamic model and by a Drude model, which assumes a rigid electron gas. While this shift is small for such a thick structure it becomes large for thinner structures as shown in Fig. 4 or 6 for instance. Such a large shift is thus a clear sign of a nonlocal response, dictated by the dispersion relation of plasmons. It gives a clear indication on the value of β . This simple model also allows to understand that, when β tends to zero, all the resonances coalesce into a single resonance, corresponding to the Ferrel resonance within the framework of the Drude model.

The fact that the even resonances of a cavity cannot be excited is a phenomenon that typically arises when a cavity is excited in phase and with the same amplitude from both sides[26], a phenomenon sometimes referred to as coherent perfect absorption[27].

At first glance, the physical situation here does not seem to fit this description because the structure is illuminated from above only. However, the slab functions as a two-mode cavity[28]. The transverse wave also traverses the semiconductor slab, and since we are very close to ω_0 , the effective refractive index approaches zero, resulting in a vanishing wavevector and a diverging wavelength. To be precise, at the considered incidence angle, the transverse wave is usually evanescent in the medium but has a very large penetration depth. In both scenarios, the slab thickness is small compared to either the wavelength or the penetration depth, allowing it to reach the bottom interface while maintaining the same

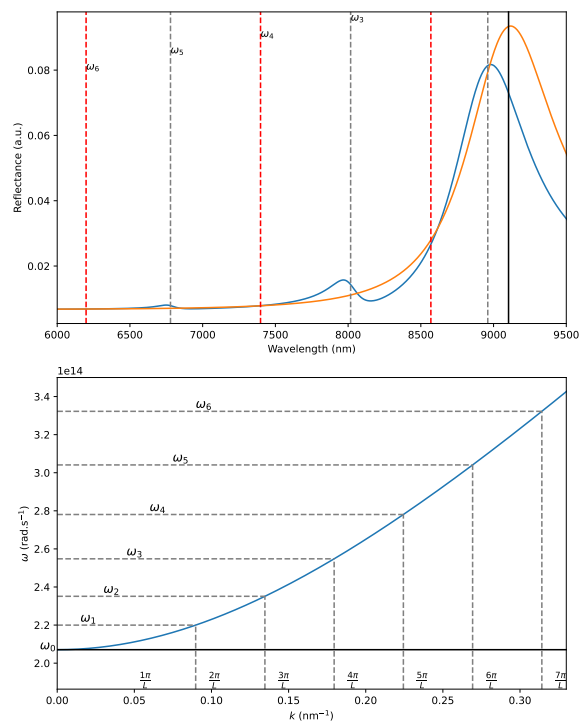


FIG. 13. Top: Simulated reflectance spectrum for a 70 nm thick slab without any imaginary part for η^2 (blue curve) and prediction using the Drude model only (orange curve). Only the odd resonances (grey dashed lines) are visible, while even resonances are absent. A simple cavity formula provides an accurate way to compute the position of these resonances, allowing to better understand all the characteristics of plasmon resonances and how they behave when changing β , the incidence angle of the thickness of the semiconductor. Bottom: Dispersion curve for plasmons, and cavity resonance conditions on k : allowing to compute the resonance frequencies.

phase and amplitude. The plasmon that is generated at the bottom interface is then expected to have the same phase as the plasmon generated at the top interface and a comparable amplitude, thus canceling the even resonances of the cavity. We underline that this also leads to the enhancement of odd resonances. This is fundamental in the so called coherent perfect absorption and explains the large absorption cross-section of plasmonic nanocavities[29] because it enhances absorption at resonance by a factor of typically four. Without such a phenomenon, it is likely only the main resonance could have been observed here.

B. Second viscosity of the electron gas

Given the narrow range of frequencies around the screened plasma frequency for which plasmon resonances can be observed, and the uncertainties regarding the imaginary part of β , it is not possible to determine which theory proposed in earlier works [8, 9, 12] is accurate by monitoring the dependency of the hydrodynamic parameter on frequency. As shown above, a constant imaginary part allows

very accurate fits of the experimental data. Moreover, we believe that a physically satisfactory explanation for the additional losses experienced by plasmons, beyond friction with the lattice, is still lacking.

The GNOR model introduces an additional diffusion current into the charge conservation equation. While this has the advantage of producing a supplementary term that can be accounted for by using a dispersive η^2 as above, the assumption of a supplementary diffusion current is a strong, unprecedented, one. It is not widely accepted.

Another approach has thus been proposed, probably inspired by the fact that in conductive 2D systems, electron gas seem to exhibit a viscous behavior[30, 31], well described by a hydrodynamic model. It consists in adding a viscous term to the hydrodynamic model[13], with a shear viscosity term[8]. When this term is taken into account however, the equations (4) are deeply modified. An imaginary part to β should ideally correspond to a term proportional to $\nabla(\nabla \cdot \mathbf{P}_f)$ whereas the viscosity adds also a $\Delta \mathbf{P}_f$ that potentially lifts the degeneracy of the plasmon leading to two distinct forms, as is sometimes incorrectly assumed[32].

We think however that there is a lot of merit in such an approach. The fact that adding a simple imaginary part to β^2 seems so accurate, as shown above, suggests strongly that a

term $\nabla(\nabla \cdot \mathbf{P}_f)$ is missing. A lot of attention has been paid to the shear viscosity, but we would like to underline that another viscosity has been overlooked: the second (or bulk) viscosity of the electron gas[33]. This form of viscosity intervenes when the fluid expands or contracts significantly. It is typically neglected when deriving the Navier-Stokes equations because most fluid flows are essentially incompressible, even if the fluid itself is very compressible, leaving shear as the only source of friction[34]. This assumption, called the Stokes hypothesis, is so common and accurate that the bulk viscosity of a gas is challenging to estimate. Furthermore, monoatomic gases are expected to have a vanishing bulk viscosity. However, bulk viscosity is the dominant source of attenuation for sound in gases, and in such cases, its value has been found to be orders of magnitude larger than that of shear viscosity[35, 36].

In the present case, the shear within the electron gas, where longitudinal waves propagate, is minimal, while the gas is primarily subjected to high-frequency compressions and expansions. This is typically a situation in which the second viscosity can be expected to dominate.

In order to see how the second viscosity can be taken into account, we consider that the electron gas is a newtonian fluid obeying to the following equation[33–35, 37] :

$$n m^* \frac{\partial \mathbf{v}}{\partial t} + n m^* \mathbf{v} \cdot \nabla \mathbf{v} = -\nabla p + \mu \Delta \mathbf{v} + (-e) n \mathbf{E} - n m^* \gamma \mathbf{v} + \xi \nabla(\nabla \cdot \mathbf{v}) \quad (11)$$

where n and m^* are the electron density and electron effective mass, respectively, \mathbf{v} the electron velocity, p the pressure inside the electron gas, μ the (shear) viscosity, γ a damping factor and ξ the second (or bulk) viscosity.

If, as explained above, shearing is minimal, we can assume that the first viscosity can be neglected. As is classically done to obtain a linear response model, \mathbf{v} is considered a first order term, so that the inertial term $\mathbf{v} \cdot \nabla \mathbf{v}$ can be neglected also. The electron gas density n can be decomposed into a constant term n_0 and a first-order fluctuation n_1 so that finally we can write $-n_0 e \partial_t \mathbf{v} \simeq \partial_t \mathbf{j}$ at the first order. This can also be done for the spatial derivatives of the bulk viscosity term. Taking these steps into account leads to

$$-\frac{m^*}{e} \partial_t \mathbf{j} = -\nabla p + \frac{m^*}{e} \gamma \mathbf{j} - n_0 e \mathbf{E} - \frac{\xi}{n_0 e} \nabla(\nabla \cdot \mathbf{j}) \quad (12)$$

The pressure term is given by quantum theories and is a power of n (usually n^3 is retained[12]). Whatever the exponent, the gradient of the pressure is simply proportional to the gradient of the electron gas density n . The nonlocal parameter β is introduced at this stage so that

$$-\nabla p = -m^* \beta^2 \nabla n. \quad (13)$$

The continuity equation can be written

$$\nabla \cdot \mathbf{j} = -\partial_t(-en) = e \partial_t n_1. \quad (14)$$

Since $\mathbf{j} = \partial_t \mathbf{P}_f$, this equation can be integrated to yield $\nabla \mathbf{P}_f = en_1$. The pressure term can be finally written

$$-\nabla p = -\frac{m^*}{e} \beta^2 \nabla(\nabla \cdot \mathbf{P}_f). \quad (15)$$

For the second viscosity term, we have:

$$-\frac{\xi}{n_0 e} \nabla(\nabla \cdot \mathbf{j}) = -\frac{\xi}{n_0 e} \partial_t \nabla(\nabla \cdot \mathbf{P}_f), \quad (16)$$

which is simply proportional to the time derivative of the pressure term. In the harmonic regime, this gives:

$$-\left(\beta^2 - \frac{i\omega\xi}{n_0 m^*}\right) \nabla(\nabla \cdot \mathbf{P}_f) - (\omega^2 - i\omega\gamma) \mathbf{P}_f = \epsilon_0 \omega_p^2 \mathbf{E}. \quad (17)$$

Thus, the second viscosity term appears exactly as the imaginary part of β^2 in the classical hydrodynamic model, with the form given above.

Formally, this is equivalent to the GNOR model, except that we do not need to assume the existence of additional diffusion currents, which is questionable and has an impact on the real part of η^2 also (the difference is however two orders of magnitude smaller than β^2 in our case). This finally would provide convincing explanation of why the negative imaginary part of β^2 acts as an additional source of dissipation. This is particularly obvious when writing the dispersion

relation for the plasmon that now becomes:

$$\omega^2 + i \left(\gamma + \frac{\xi \mathbf{k}^2}{n_0 m^*} \right) \omega = \omega_0 + \beta^2 \mathbf{k}^2. \quad (18)$$

The magnitude of the supplementary losses is expected to increase with the wavevector, and thus with the order of the resonance.

Using the improved parameter retrieval method described above, we obtained ξ values of 2.11×10^{-10} Pa.s for sample #1 with a doping of 5.31×10^{18} cm $^{-3}$ and 5.7×10^{-10} Pa.s for sample #2 at higher frequencies due to a larger doping level of approximately 1.2×10^{19} cm $^{-3}$. Despite the difficulty in comparing these values due to differing electron gas densities, they both demonstrate a notable consistency.

These values of the bulk viscosity are particularly low compared to polyatomic gases, for which measurements have been made[35]. Assuming an electron gas shares some characteristics with a monoatomic gas, such a low value is reasonable: monoatomic gases are the only ones that are expected to satisfy Stokes' hypothesis, leading to zero bulk viscosity[36], because they lack rotational or vibrational freedom degrees. The fact that an electron gas nonetheless exhibits a second viscosity suggests that a microscopic theory for bulk viscosity in an electron gas is notably lacking. We suspect the states available for the electrons in the conduction band play a role similar to the available freedom degrees in polyatomic gases. Additionally, although ξ itself is low, the electron gas in a doped semiconductor is highly tenuous, so the ratio of ξ to mass density remains high. This explains why it plays such an important role here.

V. CONCLUSION AND PERSPECTIVES

We have proposed a setup that maximizes the visibility of plasmon resonances in highly doped semiconductors. Combined with the numerical methods detailed in this work, our findings show that the hydrodynamic model, with a complex nonlocal parameter β^2 , is remarkably sufficient to capture the optical response of these materials with a high level of accuracy. This suggests that no additional mechanisms or adjustments are necessary beyond this model to fully describe the observed phenomena. We have also identified a physically consistent origin for the imaginary part of β^2 , grounded in the bulk viscosity (or second viscosity) of the electron gas, offering a convincing and straightforward justification for the well-known GNOR model[9, 38, 39].

We have also introduced a retrieval technique based on an adapted cost function (allowing to quantify the distance between the experimental data and the simulations) and the use of a global optimization algorithm. In the theoretical framework we propose, this technique allows for the estimation of the doping level, the effective mass of electrons and even the bulk viscosity of the electron gas with a single optical measurement - without any abacus. Additionally, we have shown that these parameters can be retrieved manually with satisfactory accuracy, provided that the resonances are clearly

identified, making the approach accessible even without advanced computational tools. These parameters can be considered sufficient to fully characterize the optical response of n-doped semiconductors.

This is particularly advantageous because many numerical methods have been developed to simulate the behavior of nonlocal materials using the hydrodynamic model, even in complex geometries[40–42]. While plasmon resonances have a strong fundamental interest, it is also crucial to highlight that spatial dispersion plays an important but distinct role below the epsilon-near-zero (ENZ) frequency. In this frequency range, highly doped semiconductors emerge as exceptional plasmonic materials capable of supporting surface waves or more complex guided modes with high effective indices (slow light), which can be exploited to design sensors for detecting and characterizing even small quantities of molecules[43, 44]. Previous studies have demonstrated that the slower the plasmonic guided mode[45], the more pronounced the impact of spatial dispersion[16, 39, 46, 47]. This effect is particularly significant near the ENZ frequency and in the presence of high refractive index materials[21], as commonly observed in the IR range where semiconductors exhibit large permittivities. Therefore, we anticipate that nonlocal effects will remain significant even below the ENZ frequency, underscoring the importance of having suitable simulation tools and parameter retrieval techniques.

Overall, spatial dispersion is often overlooked, not only in the study of doped semiconductors and metals but also in ENZ materials more generally. In these materials, which are typically treated as purely local, predictions of unusual and surprising effects have been made[48]. However, as discussed here, relying on a local description involves assuming a somewhat rigid behavior of the electron gas around the ENZ frequency, effectively implying an infinite propagation speed for longitudinal waves. The inclusion of spatial dispersion may alter these predictions and lead to more accurate conclusions.

Despite the challenges in observing nonlocal effects in metals within the visible range, significant efforts have been made over the past decade to develop theoretical and numerical tools and to design structures that maximize these effects. It is striking how these advancements are now proving to be highly relevant for highly doped semiconductors. Given the crucial role of spatial dispersion in these materials, as discussed above, it seems likely that spatial dispersion will soon become a standard approach for describing their optical response. We are pleased to see this area of research transition from a purely theoretical curiosity to a practical, widely-adopted tool and are convinced that this shift will help to answer the remaining fundamental questions.

ACKNOWLEDGMENTS

This work has been partially funded by the French “Investment for the Future” program (EquipEx EXTRA, ANR 11-EQPX-0016), and by the French ANR (Nano-Elastir, 19-ASTR-0003-02; SWAG-P 23-CE09-0014).

- [1] P. Drude, Zur elektronentheorie der metalle, *Annalen der physik* **306**, 566 (1900).
- [2] L. Tonks and I. Langmuir, Oscillations in ionized gases, *Physical Review* **33**, 195 (1929).
- [3] R. A. Ferrell and E. A. Stern, Plasma resonance in the electro-dynamics of metal films, *Journal of Quantitative Spectroscopy and Radiative Transfer* **2**, 679 (1962).
- [4] T. Taliercio, V. N. Guilengui, L. Cerutti, E. Tournié, and J.-J. Gréffet, Brewster “mode” in highly doped semiconductor layers: an all-optical technique to monitor doping concentration, *Optics express* **22**, 24294 (2014).
- [5] A. R. Melnyk and M. J. Harrison, Resonant excitation of plasmons in thin films by electromagnetic waves, *Physical Review Letters* **21**, 85 (1968).
- [6] A. R. Melnyk and M. J. Harrison, Theory of optical excitation of plasmons in metals, *Physical Review B* **2**, 835 (1970).
- [7] T. Golestanizadeh, A. Zarifi, T. Jalali, J. R. Maack, and M. Wubs, Hydrodynamic acoustic plasmon resonances in semiconductor nanowires and their dimers, *JOSA B* **36**, 2712 (2019).
- [8] D. De Ceglia, M. Scalora, M. A. Vincenti, S. Campione, K. Kelley, E. L. Runnerstrom, J.-P. Maria, G. A. Keeler, and T. S. Luk, Viscoelastic optical nonlocality of low-loss epsilon-near-zero nanofilms, *Scientific reports* **8**, 1 (2018).
- [9] N. A. Mortensen, S. Raza, M. Wubs, T. Søndergaard, and S. I. Bozhevolnyi, A generalized non-local optical response theory for plasmonic nanostructures, *Nature communications* **5**, 3809 (2014).
- [10] A. Vasanelli, S. Huppert, A. Haky, T. Laurent, Y. Todorov, and C. Sirtori, Semiconductor quantum plasmonics, *Physical Review Letters* **125**, 187401 (2020).
- [11] J. Benedicto, R. Pollès, C. Ciraci, E. Centeno, D. R. Smith, and A. Moreau, Numerical tool to take nonlocal effects into account in metallo-dielectric multilayers, *JOSA A* **32**, 1581 (2015).
- [12] P. Halevi, Hydrodynamic model for the degenerate free-electron gas: generalization to arbitrary frequencies, *Physical Review B* **51**, 7497 (1995).
- [13] C. Ciraci, J. B. Pendry, and D. R. Smith, Hydrodynamic model for plasmonics: A macroscopic approach to a microscopic problem, *ChemPhysChem* **14**, 1109 (2013).
- [14] H. Bhatia, G. Norgard, V. Pascucci, and P.-T. Bremer, The helmholtz-hodge decomposition—a survey, *IEEE Transactions on visualization and computer graphics* **19**, 1386 (2012).
- [15] E. Sakat, A. Moreau, and J.-P. Hugonin, Generalized electromagnetic theorems for nonlocal plasmonics, *Physical Review B* **103**, 235422 (2021).
- [16] A. Moreau, C. Ciraci, and D. R. Smith, Impact of nonlocal response on metallodielectric multilayers and optical patch antennas, *Phys. Rev. B* **87**, 045401 (2013).
- [17] M. Burda, I. Richter, and P. Kwiecien, Nonlocal response of planar plasmonic layers, *Optical and Quantum Electronics* **55**, 1286 (2023).
- [18] W. Steinmann, Experimental verification of radiation of plasma oscillations in thin silver films, *Physical Review Letters* **5**, 470 (1960).
- [19] M. Anderegg, B. Feuerbacher, and B. Fitton, Optically excited longitudinal plasmons in potassium, *Physical Review Letters* **27**, 1565 (1971).
- [20] E. D. Palik, *Handbook of optical constants of solids*, Vol. 3 (Academic press, 1998).
- [21] A. Pitelet, N. Schmitt, D. Loukrezis, C. Scheid, H. De Gersem, C. Ciraci, E. Centeno, and A. Moreau, Influence of spatial dispersion on surface plasmons, nanoparticles, and grating couplers, *JOSA B* **36**, 2989 (2019).
- [22] M. A. Barry, V. Berthier, B. D. Wilts, M.-C. Cambourieux, P. Bennet, R. Pollès, O. Teytaud, E. Centeno, N. Biais, and A. Moreau, Evolutionary algorithms converge towards evolved biological photonic structures, *Scientific reports* **10**, 12024 (2020).
- [23] P. Bennet, D. Langevin, C. Essoual, A. Khaireh-Walieh, O. Teytaud, P. Wiecha, and A. Moreau, Illustrated tutorial on global optimization in nanophotonics, *JOSA B* **41**, A126 (2024).
- [24] D. Langevin, P. Bennet, A. Khaireh-Walieh, P. Wiecha, O. Teytaud, and A. Moreau, Pymoosh: a comprehensive numerical toolkit for computing the optical properties of multilayered structures, *JOSA B* **41**, A67 (2024).
- [25] A. Moreau, D. Langevin, Teytaud, P. Bennet, and P. Chevalier, Anmoreau/pymoosh: Get always closer to 4.0 (2024).
- [26] C. Lemaître, E. Centeno, and A. Moreau, Interferometric control of the absorption in optical patch antennas, *Scientific Reports* **7**, 2941 (2017).
- [27] D. G. Baranov, A. Krasnok, T. Shegai, A. Alù, and Y. Chong, Coherent perfect absorbers: linear control of light with light, *Nature Reviews Materials* **2**, 1 (2017).
- [28] A. Pitelet, É. Mallet, E. Centeno, and A. Moreau, Fresnel coefficients and fabry-perot formula for spatially dispersive metallic layers, *Physical Review B* **96**, 041406 (2017).
- [29] A. Moreau, C. Ciraci, J. J. Mock, R. T. Hill, Q. Wang, B. J. Wiley, A. Chilkoti, and D. R. Smith, Controlled-reflectance surfaces with film-coupled colloidal nanoantennas, *Nature* **492**, 86 (2012).
- [30] D. Bandurin, I. Torre, R. K. Kumar, M. Ben Shalom, A. Tomadin, A. Principi, G. Auton, E. Khestanova, K. Novoselov, I. Grigorieva, *et al.*, Negative local resistance caused by viscous electron backflow in graphene, *Science* **351**, 1055 (2016).
- [31] M. Polini and A. K. Geim, Viscous electron fluids, *Physics Today* **73**, 28 (2020).
- [32] S. Raza, G. Toscano, A.-P. Jauho, M. Wubs, and N. A. Mortensen, Unusual resonances in nanoplasmonic structures due to nonlocal response, *Physical Review B—Condensed Matter and Materials Physics* **84**, 121412 (2011).
- [33] R. E. Graves and B. M. Argrow, Bulk viscosity: past to present, *Journal of Thermophysics and Heat Transfer* **13**, 337 (1999).
- [34] G. Buresti, A note on stokes’ hypothesis, *Acta Mechanica* **226**, 3555 (2015).
- [35] R. L. Ash, A. J. Zuckerwar, and Z. Zheng, *Second coefficient of viscosity in air*, Tech. Rep. No. NASA-CR-187783 (NASA, 1991).
- [36] M. S. Cramer, Numerical estimates for the bulk viscosity of ideal gases, *Physics of fluids* **24** (2012).
- [37] M. Gad-el Hak, Stokes’ hypothesis for a newtonian, isotropic fluid, *Journal of Fluids Engineering* **117**, 3 (1995).
- [38] S. Raza, S. I. Bozhevolnyi, M. Wubs, and N. A. Mortensen, Non-local optical response in metallic nanostructures, *Journal of Physics: Condensed Matter* **27**, 183204 (2015).
- [39] S. Boroviks, Z.-H. Lin, V. A. Zenin, M. Ziegler, A. Dellith, P. Gonçalves, C. Wolff, S. I. Bozhevolnyi, J.-S. Huang, and N. A. Mortensen, Extremely confined gap plasmon modes: when nonlocality matters, *Nature Communications* **13**, 3105 (2022).
- [40] G. Toscano, S. Raza, A.-P. Jauho, N. A. Mortensen, and M. Wubs, Modified field enhancement and extinction by plasmonic nanowire dimers due to nonlocal response, *Opt. Express* **20**, 4176 (2012).

- [41] N. Schmitt, C. Scheid, S. Lanteri, A. Moreau, and J. Viquerat, A dgtd method for the numerical modeling of the interaction of light with nanometer scale metallic structures taking into account non-local dispersion effects, *Journal of Computational Physics* **316**, 396 (2016).
- [42] P. Kwiecien, M. Burda, and I. Richter, Nonlocal fourier modal method for analyzing nonlocal plasmonic periodic nanostructures, *JOSA B* **40**, 491 (2023).
- [43] R. Smaali, T. Taliercio, A. Moreau, and E. Centeno, Reshaping plasmonic resonances using epsilon-near-zero materials for enhanced infrared vibrational spectroscopy, *Applied Physics Letters* **119** (2021).
- [44] L. Paggi, A. Fabas, H. El Ouazzani, J.-P. Hugonin, N. Fayard, N. Bardou, C. Dupuis, J.-J. Greffet, and P. Bouchon, Over-coupled resonator for broadband surface enhanced infrared absorption (seira), *Nature Communications* **14**, 4814 (2023).
- [45] R. Ajib, A. Pitelet, R. Pollès, E. Centeno, Z. Ajaltouni, and A. Moreau, The energy point of view in plasmonics, *JOSA B* **36**, 1150 (2019).
- [46] S. Raza, T. Christensen, M. Wubs, S. I. Bozhevolnyi, and N. A. Mortensen, Nonlocal response in thin-film waveguides: loss versus nonlocality and breaking of complementarity, *Physical Review B—Condensed Matter and Materials Physics* **88**, 115401 (2013).
- [47] M. Khalid, O. Morandi, P. Hervieux, G. Manfredi, and C. Ciraci, Influence of the electron spill-out and nonlocality on gap plasmons in the limit of vanishing gaps, *Physical Review B* **104**, 155435 (2021).
- [48] M. Silveirinha and N. Engheta, Tunneling of electromagnetic energy through subwavelength channels and bends using ε -near-zero materials, *Physical review letters* **97**, 157403 (2006).